Original Article

High temperature performance of 316L steel reinforced by particle inoculation and processed by laser powder bed fusion

Adriana Eres-Castellanos [a,b], Ana Santana [a], Luis Miguel Sanz-Moral [c], Rosalia Rementeria [c], Rebeca Hernández Pascual [d], Marta Serrano [d], Isaac Toda-Caraballo [a], Jose A. Jimenez [a], Francisca G. Caballero [a,*], Carlos Capdevila [a]

[a] Department of Physical Metallurgy, National Center for Metallurgical Research (CENIM-CSIC), Spain
[b] Colorado School of Mines, Metallurgical and Materials Engineering, 920 15th St, Golden 80401, USA
[c] ArcelorMittal Global R&D SLab—Steel Labs, Calle Marineros 4, 33490, Avilés, Spain
[d] Centro de Investigaciones Energéticas, Medioambientales y Tecnológicas (CIEMAT), Avda Complutense 40, Madrid, 28040, Spain

ABSTRACT

Grade 316 L is one of the most versatile austenitic stainless-steel products whose potential in laser powder bed fusion has been recently evaluated. A way of improving its properties is to add reinforcements, such as TiC nanoparticles, to promote dispersion hardening. However, it is often difficult to assess microstructure-mechanical property relationships, since particle inoculation promotes heterogeneous nucleation of equiaxed grains during rapid solidification. In this work, two 316 L samples were manufactured by laser powder bed fusion, where the powder of one of them was inoculated with TiC nanoparticles. The effect of inoculants on the microstructure and its high temperature behavior was assessed. Electron Probe Micro Analyzer proved that inoculants did not get dissolved during the printing process and they predominately lay in the intercellular regions, which were solute enriched. Advanced characterization proved that inoculation did not affect the solidification structure, which remained cellular and with a similar size, or the grain size, although it did modify the bulk texture. Finally, the effect of dispersion hardening on the behavior at high temperature of a 316 L steel was evaluated by small punch tests, which proved that the addition of TiC improves all, ductility, yield strength and ultimate tensile strength at high temperature. Moreover, samples processed by LPBF showed high temperature behavior and superior strength and ductility, as compared to the ones obtained in a reference annealed steel, even though the grain size obtained in the former case was at least 50 times larger than the one obtained for the reference condition.

1.   Introduction

Laser powder bed fusion (LPBF) is a novel additive manufacturing technique that consists in the sequential deposition and melting of powder layers. LPBF enables to obtain complex part designs with low material waste [1,2]. One of the steels to be processed more extensively by this technique is 316 L [3], an austenitic stainless steel with low carbon, high additions of Ni and Cr and lower fractions of Mn and Mo. Among its applications, one can highlight chemical industries, process industries, power generation, oil, gas and construction industries, as it presents excellent corrosion resistance and moderate strength and creep resistance [4—6].

A traditional way of further improving 316 L properties is to add particles to the material to strengthen it by dispersion hardening, such as TiN [7]. However, the inoculation of particles during LPBF processes also affects the solidification structure. For example, particle inoculation can lead to grain refinement, since particles act as heterogeneous nucleation sites for equiaxed grains [8,9]. Although grain refinement is normally beneficial, as it strengthens the alloy by the Hall Petch effect [10,11], it may negatively affect creep behavior, e.g. some studies have reported minimum steady state creep rate at intermediate grain sizes [12,13]. It is therefore interesting to study isolatedly how the presence of these particles affects high temperature performance, ruling out side effects, such as grain size modification. Previous studies have shown there is a correlation between the amount of inoculant added to the powder and the grain refinement level, and have found that below a certain level, inoculants do not significantly affect grain size [14]. Therefore, if grain refinement is not desired, the amount of inoculated particles must be kept low.

Therefore, the aim of this study is to evaluate the effect of particles on the creep behavior of a 316 L steel. To do so, two different types of powder were used: 316 L steel powder and 316 L steel powder inoculated with a small fraction of 0.5 wt.% of TiC nanoparticles. A hot rolled steel subjected to an annealing treatment in the range 1050—1100 °C, was used as a reference. Advanced characterization techniques, such as Scanning Electron Microscopy (SEM), Electron Probe Micro Analyzer (EPMA), X-Ray Diffraction (XRD) or Electron Back-scattered Diffraction (EBSD) were used to make sure that inoculated particles had not been dissolved during the printing process and to study the effect of TiC precipitates on solidification structure, grain size and crystallographic texture. Moreover, the role of dispersion hardening on the material high temperature properties were evaluated by small punch tests. Although 316 L steels have been studied by small punch tests in the past by several authors [15—18], they have not been used before to characterize LPBF samples.

2.   Experimental

In this work, commercial 316 L steel was selected to study the effect of processing and particle inoculation on the
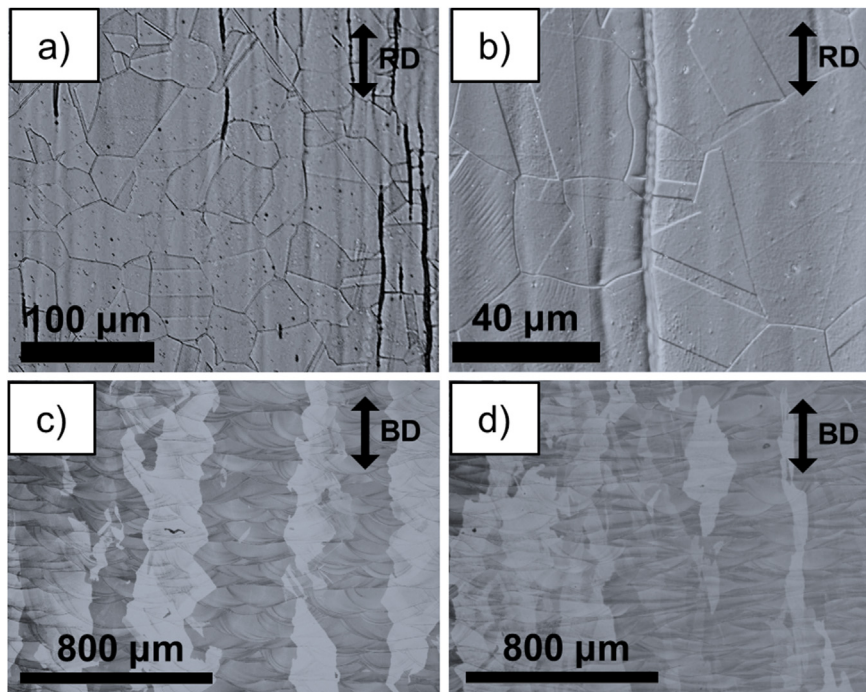

Fig. 1 − (a, b) SEM micrographs corresponding to the reference annealed microstructure; (c, d) OM micrographs showing the melt pools and the grain growth on the LPBF-316 L (c) and the LPBF-316 L + TiC conditions. Micrographs correspond to the longitudinal section, where the rolling or building direction, RD and BD, respectively, are represented by an arrow on the right top part.

microstructure and high temperature performance. The first of the conditions, called reference from now on, was a hot rolled steel subjected to an annealing treatment in the range 1050−1100 °C in the frame of the project EUROTRANS [19].

Two other conditions were processed by LPBF by using a TruPrint1000 printer, where the first one, named LPBF-316 L, was built with 316 L powder, whereas the second one, LPBF-316 L + TiC, was built with 316 L powder inoculated with TiC nanoparticles. Although 0.5 wt.%, of nanoparticles was used, it is very likely that the final weight percentage was lower, as some particles may have gotten lost during the process. Both samples were processed under an Ar atmosphere and built as cylinders with a height and diameter of 16 and 4.5 mm, respectively, by using a stripe unconnected strategy with a hatch spacing of 0.2 mm. The laser scan was 100 mm/s, the layer thickness was 50 μm and the stripe width was 4 mm. The scanning direction was sequentially rotated by 45° from layer to layer. The laser emission mode was continuous wave and the laser power was 170 W.

The LPBF samples were prepared by standard metallographic procedures and observed at low magnification by inspecting the sample longitudinal (L) section (parallel to the building direction, BD) under an optical microscope (OM). Image compositions of the whole L section were formed and
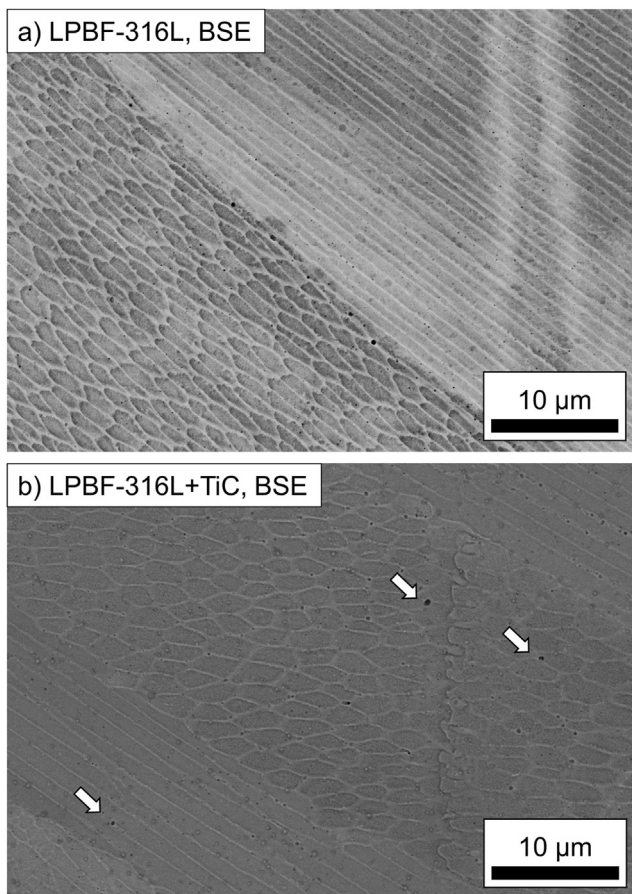

Fig. 2 − Solidification structure obtained by processing the 316 L (a) and the 316 L + TiC (b) powder by LPBF with the selected set of printing parameters. Imaging was performed by SEM, using backscattered electrons. TiC particles are highlighted by arrows.

post-processed by ImageJ [20] to estimate the porosity. In order to reveal the melt pool boundaries, microstructures were electrochemically etched for 60 s by using 2% oxalic acid as electrolyte and a plate of stainless steel as cathode. Although a voltage of 20 V was set, it was proven that, during the etching, the real voltage dropped to 4 V due to the resistance of the system. Subsequently, the solidification structures were characterized by using a Hitachi S 48000 J SEM operating at 15 kV on backscattered electron mode, with a working distance of 8.5 mm.

After subjecting the samples to an additional polishing step to remove the etched layer, EPMA measurements were performed in the LPBF-316 L + TiC condition in a JEOL Superprobe JXA 8900 M operating at 20 kV. EPMA intensity maps had to be post-processed applying a filter to minimize the noise measurements intrinsic to the raw data, since such noise induces that the measured sum of composition at each scanned point varies between 95 at. % and 105 at. % [21]. The filter uses a smooth function to reach a composition close to 100 at. % at all scanned points, using in this work a smoothing of order 3 to avoid excessive loss of information (see appendix A of [21] for a detailed explanation). This enabled an appropriate visualization of the EPMA measurements, since it highlights the main compositional variations in the microstructure, wherever they exist.

Afterwards, X-Ray Diffraction texture measurements were performed by a Bruker AXS D8 X-ray diffractometer, with a Co X-ray tube working at 40 KV and 30 mA and equipped with a LynxEye Linear Position Sensitive Detector. Incomplete pole figures (PF), (111), (200) (220) and (311) were measured on the transverse (T) section in the back-reflection mode in the range of pole distance from 0 to 70°. A measuring time of 15 s per measuring interval in steps of 5° was used. The background contribution was eliminated using measurements taken far enough from the peak edge on the side of each reflection, and the correction of defocusing was performed using a random standard prepared by hot isostatic pressing. The experimental pole figures were analyzed using the program Diffrac. Texture (Bruker AXS). The orientation distribution function (ODF) was derived by the use of the Bunge's series expansion method ($l_{MAX} = 22$) and subsequently ghost corrected [22]. The sample reference system imposed upon the calculation of the orientation distribution function was orthorhombic, corresponding to the symmetry observed in the pole figures. ODF data was represented by the φ_2 sections at 45, 65 and 90° obtained with the help of the MATLAB toolbox called MTEX [23], since the most important orientations for fcc materials are included in these sections.

The grain structure was observed by EBSD measurements, conducted in a Zeiss Auriga Compact Focused Ion Beam (FIB) − SEM operating at 20 kV. During data collection, samples were tilted by 70°. Areas of 1152×861 μm^2 were scanned by using a step size of 3 μm. Only fcc was considered. Indexation percentages above 80% were achieved. EBSD data was cleaned and plot with the MatLab® toolbox MTEX [23].

Finally, the mechanical properties at high temperature of the reference, the LPBF-316 L and the LPBF-316 L + TiC samples were evaluated by Small Punch Tests using a self-developed test device. The description of this technique can be found elsewhere [24−28]. Experiments were performed in
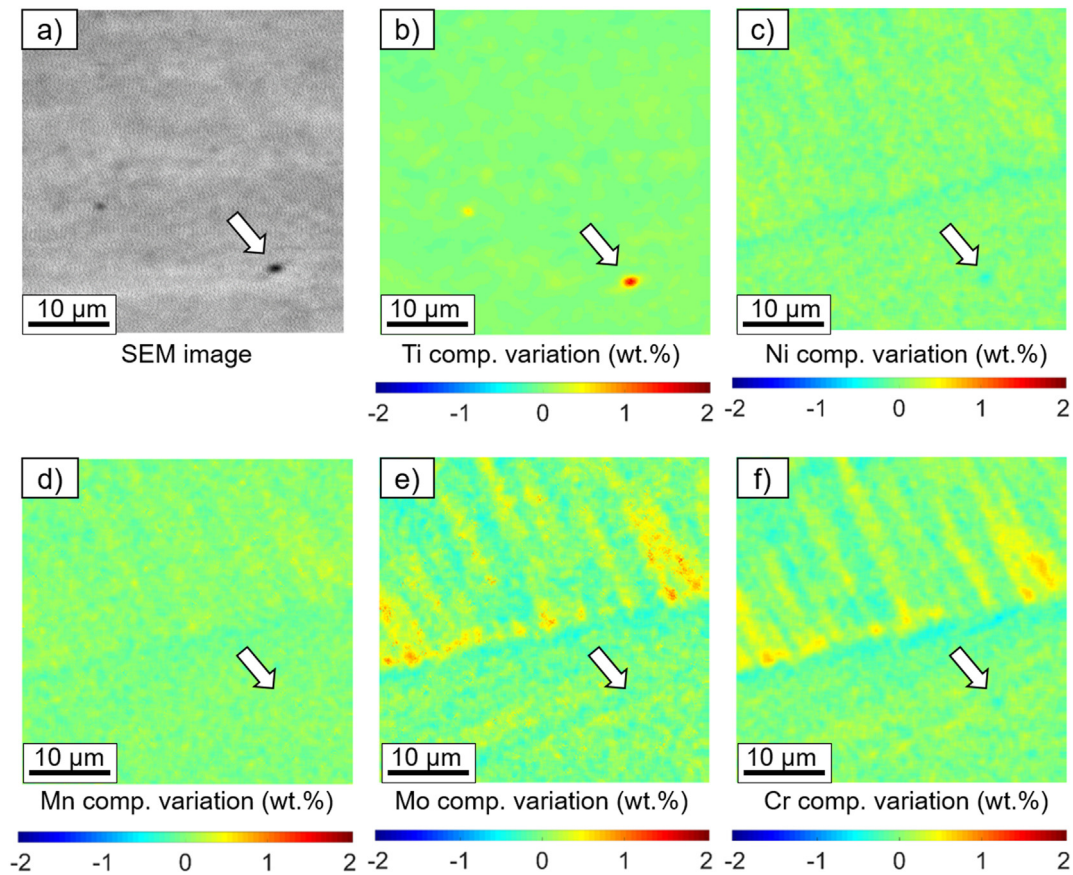
Fig. 3 − For the LPBF-316 L + TiC, (a) correlative SEM image and EPMA intensities corresponding to different elements: (b) Ti, (c) Ni, (d) Mn, (e) Mo and (f) Cr. The observed TiC particle is pointed by an arrow.
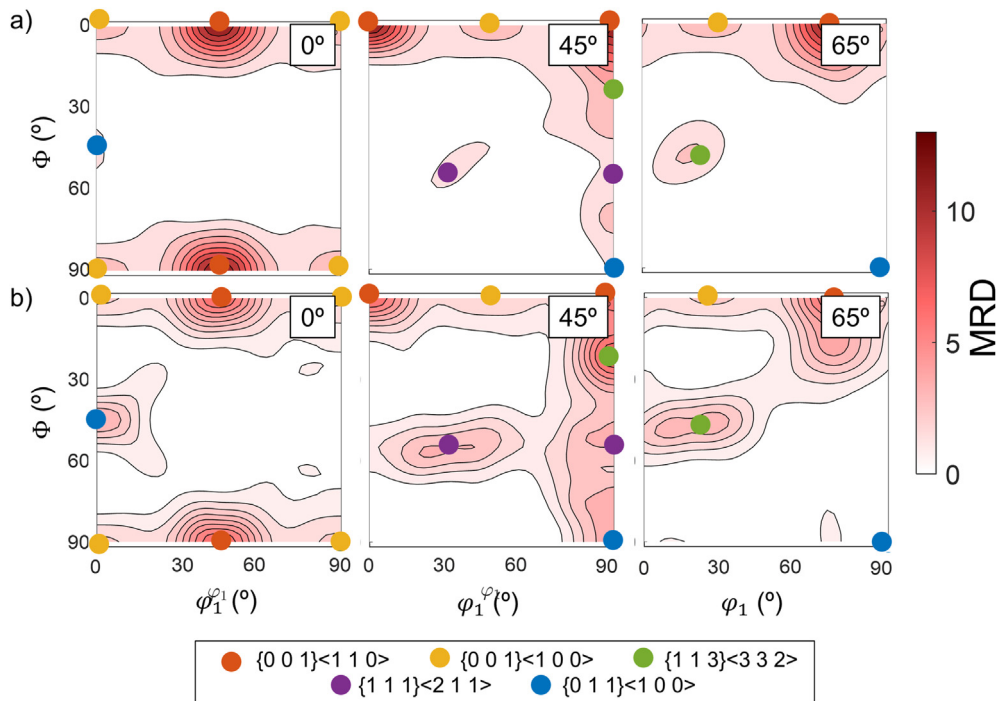

Fig. 4 − $\varphi_2 = 0°$, $\varphi_2 = 45°$ and $\varphi_2 = 65°$ ODF sections corresponding to the microstructures obtained by processing the 316 L (a) and the 316 L + TiC (b) powder by LPBF with the selected set of printing parameters. The identified texture components (with a tolerance of 15°) are identified by circles on the sections. Intensity is represented in MRD, Multiples of Random Distribution.
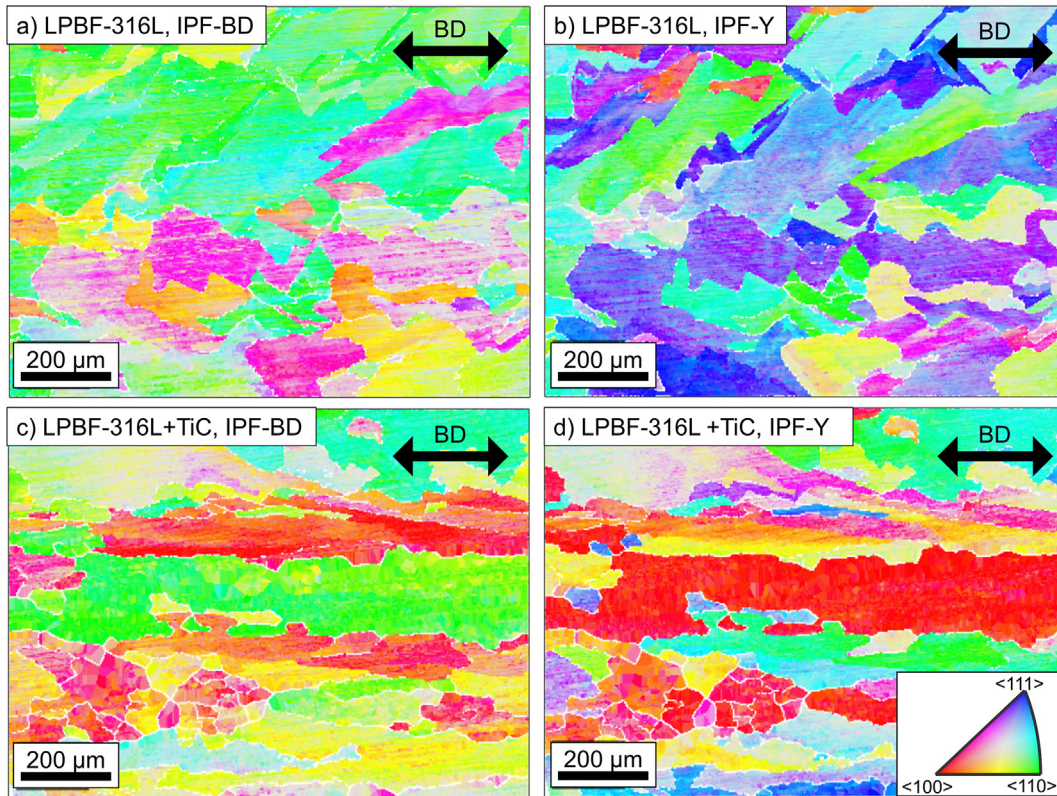
Fig. 5 – EBSD maps taken on the longitudinal sections of the conditions LPBF-316 L (a, b) and LPBF-316 L + TiC (c, d). Coloring corresponds to the Inverse Pole Figure (IPF) values along the building direction (BD – a, c) and the vertical direction (Y – b, d).

the Centro de Investigaciones Energéticas, Medioambientales y Tecnológicas (CIEMAT), following the standard from the European Committee for Standardization (CEN), see Ref. [29] and the standard UNE-EN 10371. Discs specimens of 0.25 mm thickness (h) and 3 mm diameter were machined from the as-built samples. Small punch tests consist in the deformation of a small disc by constant displacement rate, while load (F) and disc deflection (u) are measured. Results are usually analyzed from the F-u curve, form which the following parameters can be extracted: F_M or maximum load, F_E or load characterizing the transition from linearity to the stage associated with the spread of the yield zone through the specimen thickness, u_M or disc deflection corresponding to maximum load and E_{SP} or fracture energy obtained from the area under the load punch displacement curve up to maximum load.

3. Results and discussion

The reference microstructure was that one corresponding to an annealing treatment, predominantly consisting of austenitic grains, as can be observed in Fig. 1(a). The austenitic
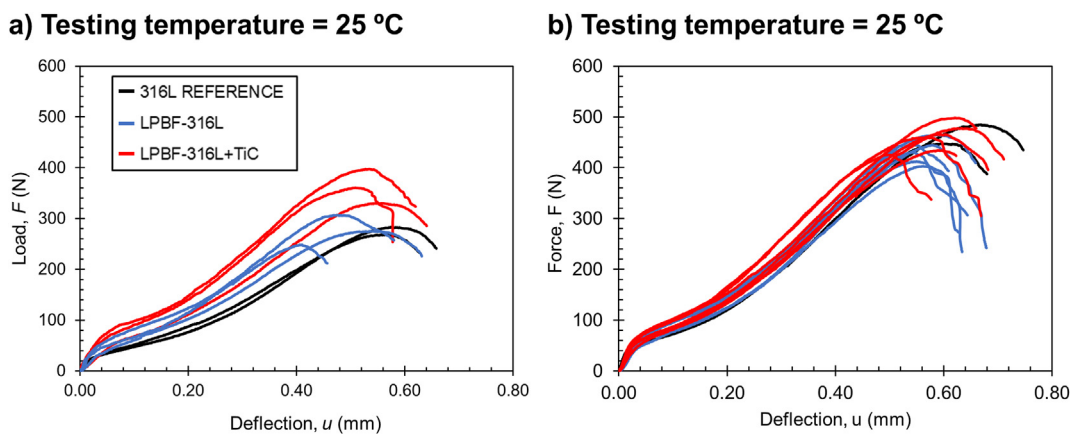

Fig. 6 – Values of F vs. u for the conditions of study: reference annealed, LPBF-316 L and LPBF-316 L + TiC, obtained for the testing temperatures of (a) 500 °C and (b) 25 °C.
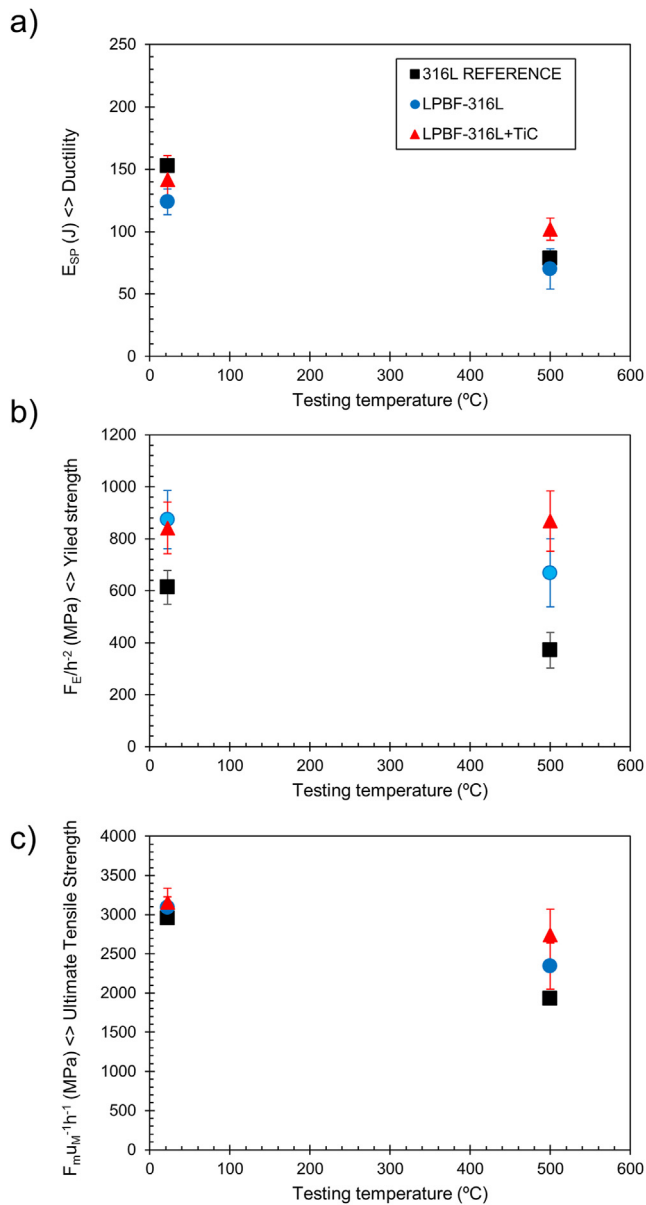
a)

b)

c)

Fig. 7 − Values of E_{SP} (a), $F_E h^{-2}$ (b) and $F_M u_M^{-1} h^{-2}$ (c) as a function of the testing temperature, for the conditions of study: reference annealed, LPBF-316 L and LPBF-316 L + TiC. Error bars represent the measurement standard error.

grains were in some cases twinned, see example in Fig. 1(b), and had an average diameter of 24 μm [19]. Moreover, a low fraction of elongated delta ferrite grains was also observed, where their longest axis is parallel to the rolling direction (RD), as can be seen in Fig. 1(a and b).

With respect to the LPBF conditions, OM image analyses enabled to conclude that the porosity of the structure associated to the selected laser power and speed was rather low, 0.1 ± 0.1%. A low magnification OM micrograph is shown in Fig. 1(c), where it can be observed how elongated grains of austenite, with a length higher than 1 mm, grow parallel to the BD across melt pools, regardless of the used powder, showing that no refinement took place when adding the TiC particles.

No delta ferrite was observed. Note that melt pools overlap, meaning that the estimation of the real dimensions of the melt pool would involve the study of a single track or the study of the last printed layer, as has been done in previous works [30,31].

Fig. 2 shows the SEM characterization performed at high magnification for both LPBF-316 L and LPBF-316 L + TiC conditions, where it can be observed how the structure solidified in the morphology of cells in both cases, where the cell size did not significantly vary as TiC nanoparticles were inoculated. The comparison of both Fig. 2(a) vs. Fig. 2(b) enables to identify that TiC nanoparticles apparently lie in the intercellular regions. An EPMA analysis was carried out to confirm this finding, see Fig. 3. It can be observed that the structure presents a significant segregation of Mo and Cr, and a slightly increase in Mn and Ni content, whereas the cellular inner regions are poor in solute. Moreover, it can be seen how a TiC particle sits in one of the intercellular regions. Note that, due to the particle size, its chemical composition may not be accurate due to overlapping with the matrix, given the EPMA resolution.

Fig. 4 shows three ODF sections of each of the studied LPBF conditions, where it can be observed how the presence of TiC particles affected macro-texture. Both conditions predominantly show rotated cube texture, with minor cube and Goss texture components, although their intensities change depending on the condition. While the intensities (in Multiples of Random Distribution, MRD) of both the cube and rotated cube components are higher for the LPBF-316 L condition, see Fig. 4(a), the Goss component is stronger in the inoculated condition, Fig. 4(b). Additionally, there are other two components which are barely visible in the ODF of the former sample, whereas they have significant MRD values for the LPBF-316 L + TiC specimen: {1 1 3}<3 3 2> and {1 1 1}<1 1 2>. In structures formed by LPBF, texture has been shown to be controlled by some process parameters, such as laser power [32], scan strategy [33] and thermal cycling [33]. These results show that particle inoculation also affects the resultant texture, for fixed processing parameters.

Fig. 5 shows the EBSD maps taken on the longitudinal sections, where coloring corresponds to the Inverse Pole Figure (IPF) values along BD and the vertical direction, respectively. Note that maps are not large enough, given the grain size, to assess texture. However, grain morphology and size can be qualitatively studied. As can be observed, grains are elongated along the BD, where their longest axis is fairly large, i.e. grains grow larger than the EBSD maps width, as previously confirmed by OM. The presence of such long grains is associated to their epitaxial growth, as has been previously reported in austenitic steels [34]. As previously mentioned, no effect of the inoculation of TiC particles on the refinement is apparently observed.

Finally, Fig. 6 shows the load F vs. displacement u curves corresponding to the different microstructures and testing temperatures. Tests were repeated several times to obtain an estimated standard error, given the noise of the results. Fig. 7 shows the room temperature and high temperature values of E_{SP} (a), F_E normalized by the square thickness of the small punch disc ($F_E h^{-2}$, b) and F_M normalized by the displacement and maximum load and the thickness of the small punch disc
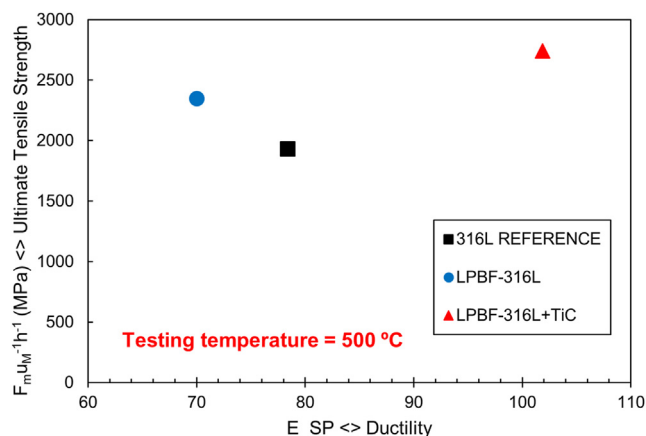
Fig. 8 − Values of $F_M u_M^{-1} h^{-2}$ versus E_{SP} for a testing temperature of 500 °C that can be correlated to a plot of ductility versus strength.

though the grain size obtained in the former case was at least 50 times larger than the one obtained for the reference condition.
e) The addition of TiC improves all, ductility, yield strength and ultimate tensile strength at temperature, as compared to the reference condition and the LPBF condition without TiC nanoparticles.

Declaration of Competing Interest

The authors declare that they have no known competing financial interests or personal relationships that could have appeared to influence the work reported in this paper.

($F_M u_M^{-1} h^{-1}$, c). These values are directly associated to the ductility, the yield strength and the ultimate tensile strength, respectively, according to the UNE-EN 10371 standard. These results indicate a higher strength at high temperature of the LPBF materials, especially for the LPBF-316 L + TiC condition. This superior strength is attributed by other authors to a combination of fine cell structure, a high dislocation density and chemical segregation in the cell walls [35]. At it has been previously discussed, the presence of TiC particles does not significantly affect the cell structure either the grain size. Hence, the enhanced strength of the LPBF-316 L + TiC condition could be attributed to dispersion hardening.

Interestingly, the higher strength obtained for the LPBF-316 L + TiC condition is not affected by the testing temperature as significantly as the one of reference 316 L and the LPBF-316 L conditions, i.e. the value of the $F_E h^{-2}$ obtained at 500 °C is close to the one obtained at room temperature, see Fig. 6(b). Fig. 8 shows the relationship between E_{SP} and $F_M u_M^{-1} h^{-1}$. In this figure, the improved strength and ductility properties of the LPBF-316 L + TiC condition at high temperature are evident, which could be attributed to a higher stability of the cell structure at high temperature due to the presence of the TiC particles [36].

4.   Conclusion

a) Processing 316 L through LPBF leads to cellular structures, where columnar austenite grains can be more than 1 mm long. Adding TiC to the powder in a small fraction (0.5 wt.%) led to neither grain refinement nor to solidification cell refinement.
b) After melting and solidifying TiC-mixed powder, nano-particles lie in the intercellular regions, that are solute-enriched.
c) TiC nanoparticle inoculation modifies the texture of the resultant microstructure, for fixed processing parameters.
d) Samples processed by LPBF show high temperature behavior and superior strength and ductility, as compared to the ones obtained in a reference annealed steel, even

REFERENCES

[1] Fayazfar Haniyeh, Salarian Mehrnaz, Rogalsky Allan, Sarker Dyuti, Russo Paola, Paserin Vlad, et al. A critical review of powder-based additive manufacturing of ferrous alloys: process parameters, microstructure and mechanical properties. Mater Des 2018;144:98−128.
[2] Mirzaali Mohammad J, Bobbert Françoise, Zadpoor Amir A, Li Yageng. Additive manufacturing of metals using powder bed-based technologies. In: Bandyopadhyay A, Bose S, editors. Addit Manuf [Internet]. CRC Press; 2019. Available from: https://www.taylorfrancis.com/books/9780429881022.
[3] Vukkum VB, Gupta RK. Review on corrosion performance of laser powder-bed fusion printed 316L stainless steel: effect of processing parameters, manufacturing defects, post-processing, feedstock, and microstructure. Mater Des 2022:110874.
[4] Chen Nan, Ma Guoqiang, Zhu Wanquan, Godfrey Andrew, Shen Zhijian, Wu Guilin, et al. Enhancement of an additive-manufactured austenitic stainless steel by post-manufacture heat-treatment. Mater Sci Eng A 2019;759:65−9.
[5] Calderón LAÁ, Rehmer B, Schriever S, Ulbricht A, Agudo Jácome L, Sommer K, et al. Creep and creep damage behavior of stainless steel 316L manufactured by laser powder bed fusion. Mater Sci Eng A 2022;830:142223.
[6] Yu Jong Min, Dao Van Hung, Yoon Kee Bong. Investigation of creep behavior of 316L stainless steel produced by selective laser melting with various processing parameters. J Mech Sci Technol 2020;34:3249−59.
[7] Poole WJ, Mitchell A, Weinberg F. Inoculating stainless steel with titanium nitride. High Temp Mater Process 1997;16:173−82.
[8] Zhai Wengang, Zhou Wei, Nai Sharon Mui Ling. Grain refinement and strengthening of 316L stainless steel through addition of TiC nanoparticles and selective laser melting. Mater Sci Eng A 2022;832:142460.
[9] Zhai Wengang, Zhou Wei, Nai Sharon Mui Ling. Grain refinement of 316L stainless steel through in-situ alloying with Ti in additive manufacturing. Mater Sci Eng A 2022;840:142912.
[10] Hall EO. The deformation and ageing of mild steel: III discussion of results. Proc Phys Soc London Sect B [Internet] 1951;64:747−53. Available from: http://iopscience.iop.org/0370-1301/64/9/303/.
[11] Petch NJ. The cleavage strength of polycristals. J Iron steel Inst 1953;174:25−8.

[12] Lee Yo Seob, Kim Dae Whan, Lee Dok Yol, Ryu Woo Seog. Effect of grain size on creep properties of type 316LN stainless steel. Met Mater Int 2001;7:107–14.

[13] Mannan SL, Samuel KG, Rodriguez P. Influence of grain size on the tensile and creep properties of a type 316 stainless steel.

[14] Zhai Wengang, Zhu Zhiguang, Zhou Wei, Nai Sharon Mui Ling, Wei Jun. Selective laser melting of dispersed TiC particles strengthened 316L stainless steel. Compos Part B Eng 2020;199:108291.

[15] Keller C, Flipon B, Diez M, Serrano M. Mechanical characterization by traction and small punch tests of ultra-fine grained AISI 316L with bimodal grain size distributions. AIP Conf Proc. AIP Publishing LLC; 2019. p. 160002.

[16] Vijayanand VD, Mokhtarishirazabad M, Peng J, Wang Y, Gorley M, Knowles DM, et al. A novel methodology for estimating tensile properties in a small punch test employing in-situ DIC based deflection mapping. J Nucl Mater 2020;538:152260.

[17] Li KS, Peng J. Effect of pre-strain on small punch creep test of 316L stainless steel at 373K. Key Eng Mater. Trans Tech Publ; 2019. p. 152–8.

[18] Song Ming, Guan Kaishu, Qin Wen, Szpunar Jerzy A, Chen Ji. Size effect criteria on the small punch test for AISI 316L austenitic stainless steel. Mater Sci Eng A 2014;606:346–53.

[19] Knebel JU, Abderrahim HA, Caron-Carles M. Transmutation of high level nuclear waste in an accelerator driven system: towards a demonstration device of industrial interest. EUROTRANS; 2010.

[20] Rasband WS. ImageJ: image processing and analysis in Java. ASCL 2012. ascl-1206.

[21] Toda-Caraballo Isaac, Jiménez José Antonio, Milenkovic Srdjan, Jimenez-Aguirre Jorge, San-Martín David. Microstructural stability of the CoCrFe2Ni2 high entropy alloys with additions of Cu and Mo. Metals (Basel) 2021;11:1994.

[22] Bunge HJ. Texture analysis in materials science. Butterworth-Heinemann; 1982.

[23] Bachmann F, Hielscher R, Schaeben H. Texture analysis with MTEX–free and open source software toolbox. Solid State Phenom. Trans Tech Publ; 2010. p. 63–8.

[24] Rodríguez C, Fernández M, Cabezas JG, García TE, Belzunce FJ. The use of the small punch test to solve practical engineering problems. Theor Appl Fract Mech 2016;86:109–16.

[25] Campitelli EN, Spätig P, Bonadé R, Hoffelner W, Victoria M. Assessment of the constitutive properties from small ball punch test: experiment and modeling. J Nucl Mater 2004;335:366–78.

[26] Ruan Y, Spätig P, Victoria M. Assessment of mechanical properties of the martensitic steel EUROFER97 by means of punch tests. J Nucl Mater 2002;307:236–9.

[27] Vivas J, Capdevila C, Altstadt E, Houska M, San-Martín D. Importance of austenitization temperature and ausforming on creep strength in 9Cr ferritic/martensitic steel. Scr Mater 2018;153:14–8.

[28] Bruchhausen M, Austin T, Holmström S, Altstadt B, Dymacek E, Jeffs P, et al. European standard on small punch testing of metallic materials. Press Vessel Pip Conf. American Society of Mechanical Engineers; 2017. V01AT01A065.

[29] WI ENSWD. Metallic materials-Small punch test method. Doc ECISS/TC; 2018. p. 101.

[30] Gunenthiram Valérie, Peyre Patrice, Schneider Matthieu, Dal Morgan, Coste Frédéric, Fabbro Rémy. Analysis of laser–melt pool–powder bed interaction during the selective laser melting of a stainless steel. J Laser Appl 2017;29:22303.

[31] Criales Luis E, Arısoy Yiğit M, Lane Brandon, Moylan Shawn, Donmez Alkan, Özel Tuğrul, et al. Predictive modeling and optimization of multi-track processing for laser powder bed fusion of nickel alloy 625. Addit Manuf 2017;13:14–36.

[32] Gokcekaya Ozkan, Ishimoto Takuya, Hibino Shinya, Yasutomi Jumpei, Narushima Takayuki, Nakano Takayoshi. Unique crystallographic texture formation in Inconel 718 by laser powder bed fusion and its effect on mechanical anisotropy. Acta Mater 2021;212:116876.

[33] Pinto FC, Aota LS, Souza Filho IR, Raabe D, Sandim HRZ. Recrystallization in non-conventional microstructures of 316L stainless steel produced via laser powder-bed fusion: effect of particle coarsening kinetics. J Mater Sci 2022;57:9576–98.

[34] Marattukalam Jithin James, Karlsson Dennis, Pacheco Victor, Beran Přemysl, Wiklund Urban, Jansson Ulf, et al. The effect of laser scanning strategies on texture, mechanical properties, and site-specific grain orientation in selective laser melted 316L SS. Mater Des 2020;193:108852.

[35] Dryepondt Sebastien, Nandwana Peeyush, Fernandez-Zelaia Patxi, List III Fred. Microstructure and high temperature tensile properties of 316L fabricated by laser powder-bed fusion. Addit Manuf 2021;37:101723.

[36] Qiu Chunlei, Al Kindi Mohammed, Aladawi Aiman Salim, Al Hatmi Issa. A comprehensive study on microstructure and tensile behaviour of a selectively laser melted stainless steel. Sci Rep 2018;8:1–16.